

# Phase-space propagation and stability analysis of the 1-dimensional Schrödinger equation for finding bound and resonance states of rotationally excited H<sub>2</sub>.

Juan S. Molano and Carlos A. Arango\*

*Department of Chemical Sciences, Universidad Icesi, Cali, Colombia*

(Dated: June 16, 2020)

A mathematical phase-space representation of the 1-dimensional Schrödinger equation is employed to obtain bound and resonance states of the rotationally excited H<sub>2</sub> molecule. The structure of the phase-space tangent field is analyzed and related to the behavior of the wave function in classically allowed and forbidden regions. In this phase-space representation, bound states behave like unstable orbits meanwhile resonance states behave similarly to asymptotically stable cycles. The lattice of quantum states of the energy-momentum diagram for H<sub>2</sub> is calculated allowing to have a global view of the energy as function of the quantum numbers. The arc length and winding number of the phase-space trajectories, as functions of the energy, are used to obtain the energy eigenvalues of bound and resonance states of H<sub>2</sub>.

## I. INTRODUCTION

The 1-dimensional time independent nonrelativistic Schrödinger equation (TISE) is a real second order linear differential equation in the position basis [1]. As a second order differential equation, 2 boundary conditions (BCs) must be specified in order to obtain a unique solution of the TISE [2]. Boundary conditions must fit the physical problem of interest, for example, Dirichlet BCs are suitable to obtain bound states meanwhile Cauchy BCs are better to obtain continuum or resonance states.

Analytical solutions of the TISE are possible only for few model systems. The rigid rotor, the harmonic oscillator, the hydrogen atom, and the Morse oscillator are some of the exactly solvable models of interest in Chemical Physics [3]. In general, it is impossible to find explicit solutions of the TISE, and numerical methods are needed. Finite differences [4–6], spectral, and pseudospectral numerical methods are broadly employed to solve Schrödinger's equation [7]. Pseudospectral methods employ a basis of spatially localized functions centered at different spatial grid points. Bound and resonance states of the TISE are efficiently obtained by pseudospectral methods like Discrete Value Representation (DVR) [8–10] and Fourier Grid Hamiltonian (FGH) [11–13]. These pseudospectral methods are better suitable for Dirichlet boundary conditions, and need of numerical strategies, as complex scaling or complex absorbing potential (CAP), to obtain resonance or continuum states [14–17]. Spectral and pseudospectral methods for solving the TISE on unbound domains, infinite or semi-infinite, are beginning to show interesting and promising results besides their complexity [18–21].

As a second order ordinary differential equation (ODE), the 1-dimensional TISE can be represented in phase space [22]. In this representation a second order ODE is replaced by a set of 2 first order ODEs with the Cauchy BCs instead of the Dirichlet BCs of the origi-

nal problem. Numerically this idea is implemented in Numerov's method to obtain both bound and resonance states [23–28].

In this paper we study the H<sub>2</sub> molecule, with rotational excitation, employing the phase-space representation of the 1-dimensional TISE. We analyze the relationship between the structure of the phase-space vector field and the onset of bound and resonance states. Bound and resonance states are obtained as trajectories in phase-space. We show that eigenstates of the TISE can be obtained by analyzing the winding number and the arc-length of the trajectories as functions of the energy.

## II. THEORY AND METHODS

The radial Schrödinger equation for a diatomic molecule with reduced mass  $\mu$ , internuclear distance  $r \in (0, \infty)$ , and rotational angular momentum  $l \in \mathbb{Z}$ ,  $l \geq 0$ , is given by

$$\left( -\frac{1}{2\mu} \frac{d^2}{dr^2} + V_l(r) \right) \psi(r) = \mathcal{E} \psi(r). \quad (1)$$

As a singular Sturm-Liouville problem, the energy spectrum of (1) consists of a countable set of eigenvalues and eigenfunctions,  $\mathcal{E}_n$  and  $\psi_n$ , and a continuum [29].

The effective potential,  $V_l(r)$ , is the sum of a Born-Oppenheimer internuclear potential energy  $V(r)$  and a centrifugal term

$$V_l(r) = V(r) + \frac{l(l+1)}{2\mu r^2}. \quad (2)$$

Typically effective potentials of diatomic molecules grow exponentially as  $r$  goes to zero due to internuclear repulsion; for very large values of  $r$ , the dissociative limit, the effective potential approaches zero from above (below) for  $l \neq 0$  ( $l = 0$ ). Figure 1 shows the effective potential of H<sub>2</sub> molecule for angular momentum  $l = 23$ . In this figure bound states display negative energies, while 2 resonance states appear with positive energy less than the maximum of the centrifugal barrier.

\* caarango@icesi.edu.co

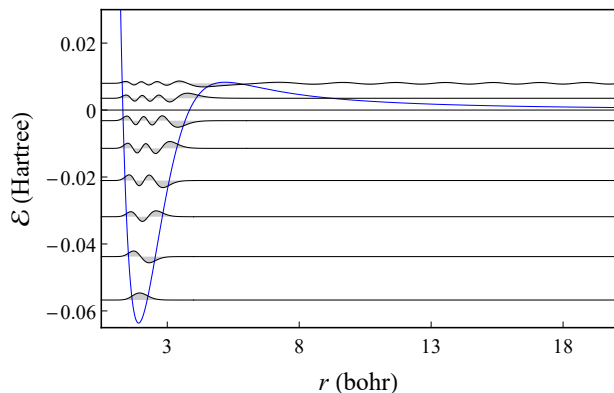


FIG. 1. H<sub>2</sub> effective potential for  $l = 23$ . Bound states (negative energy) and resonance states are shown.

Equation (1) can be written as a linear system of first order differential equations in the phase-space  $\{\psi, \dot{\psi}\}$ :

$$\dot{\psi}(r) = \varphi(r), \quad (3a)$$

$$\dot{\varphi}(r) = -k_l^2 \psi(r), \quad (3b)$$

with the dotted symbol representing  $r$  derivative,  $d/dr$ , and  $k_l = k_l(r, \mathcal{E})$  given by

$$k_l = \sqrt{2\mu(\mathcal{E} - V_l(r))}. \quad (4)$$

Equations (3) can be expressed in matrix fashion by defining the phase-space vector  $\Phi = \{\psi, \varphi\}$ ,

$$\dot{\Phi} = A_l(r, \mathcal{E})\Phi, \quad (5)$$

with

$$A_l(r, \mathcal{E}) = \begin{pmatrix} 0 & 1 \\ -k_l^2 & 0 \end{pmatrix}. \quad (6)$$

Equation (5) is an initial value problem, its solutions  $\Phi = \Phi(r, \Phi_i, \mathcal{E})$ , are  $r$ -parametric phase curves or trajectories. These trajectories are functions of the initial conditions  $\Phi_i = \{\psi(r_i), \varphi(r_i)\}$  and the energy  $\mathcal{E}$ . Equations (3) and (5) define the tangent vector field  $\dot{\Phi} = \{\dot{\psi}(r), \dot{\varphi}(r)\}$ .

The fixed points of system (5) are given by the solutions,  $\Phi^*$ , of  $\dot{\Phi}(\Phi^*) = 0$  [30]. An inspection of equations (3) shows that there is a single fixed point  $\Phi^*$  at the origin,  $\Phi^* = \{0, 0\}$ . The stability of  $\Phi^*$  depends on the eigenvalues of matrix  $A_l$ ,

$$\lambda_{1,2} = \mp i k_l. \quad (7)$$

The fixed point  $\Phi^*$  is elliptic for classically accessible regions,  $\mathcal{E} > V_l(r)$ , or hyperbolic for classically forbidden regions,  $\mathcal{E} < V_l(r)$ . At classical turning points,  $\mathcal{E} = V_l(r)$ , the eigenvalues of  $A_l$  are both zero,  $\lambda_{1,2} = 0$ . An inspection of equation (3) shows that at the classical turning points, there are lines of non isolated fixed points in

phase-space with constant  $\varphi$ , this can be seen in figure 2(b).

The eigenvectors of  $A_l$ , can be expressed in terms of the eigenvalues  $\lambda_{1,2}$ ,

$$\mathbf{e}_{1,2} = \left\{ \frac{1}{\lambda_{1,2}}, 1 \right\}. \quad (8)$$

For classically forbidden values of  $r$ , the positive (negative) eigenvector  $\mathbf{e}_1$  ( $\mathbf{e}_2$ ) defines the unstable (stable) subspace at a given value of  $r$ . The unstable and stable subspaces, for a given  $r$ , are straight lines aligned with  $\mathbf{e}_1$  and  $\mathbf{e}_2$  respectively. For the effective potential of figure 1, as  $r$  goes to zero the eigenvectors  $\mathbf{e}_{1,2}$  tend to align with the vectors  $\{0^\pm, 1\}$ . As shown in figure 2, for a given value of  $r$ , the unstable (stable) subspace resembles a straight line with positive (negative) slope and zero intercept. The slope of the stable and unstable eigenvectors tends to zero as the value of  $r$  approaches classical turning points. For classically accessible regions, eigenvalues are complex conjugate pairs, and trajectories in phase-space follow elliptic orbits around the origin.

Equations (5) are propagated from an initial  $r = r_i \approx 0$ , located in the classically forbidden region. For a fixed initial condition  $\Phi_i = \Phi(r_i) = \{0, 1\}$  in the unstable subspace, equations (5) produce a 1-parameter family of trajectories,  $\Phi(\mathcal{E}) = \Phi(r, \Phi_i, \mathcal{E})$ . In general, the  $\Phi(\mathcal{E})$  are divergent for negative energies, except at the exact energy of the eigenstates. Figure 3 displays the phase space trajectories  $\Phi(\mathcal{E}_0 \mp \Delta\mathcal{E})$  corresponding to energies below or above the ground state energy,  $\mathcal{E}_0$ . The trajectory  $\Phi(\mathcal{E}_0 - \Delta\mathcal{E})$  diverges upwards meanwhile  $\Phi(\mathcal{E}_0 + \Delta\mathcal{E})$  diverges downwards. As  $\Delta\mathcal{E}$  tends to zero, the divergence of  $\Phi(\mathcal{E}_0 \mp \Delta\mathcal{E})$  occurs closer to the fixed point  $\Phi^*$ . It is interesting to notice how the behavior of trajectories  $\Phi(\mathcal{E} \mp \Delta\mathcal{E})$  around eigenenergies resembles the behavior of unstable orbits of dynamical systems [30].

### III. RESULTS

The  $X^1\Sigma_g^+$  electronic state of H<sub>2</sub> molecule is modeled by a Born-Oppenheimer potential energy curve,  $V(r)$ . This electronic curve is obtained by spline interpolations of 3 energy data reported for different ranges of the interatomic distance  $r$ . Sims and Hagstrom [31] in the range  $0.4 \leq r/a_0 \leq 6.0$ , Wolniewicz [32] for  $6.0 < r/a_0 \leq 10.0$ , and Wolniewicz [33] for  $10.0 < r/a_0 \leq 20.0$ .

The numerical propagation of the equation (3) is performed by using the `NDSolve` function of Wolfram Mathematica. The fifth-order Explicit Runge-Kutta method is used with a variable step size ranging from  $10^{-6}$  to  $10^{-3}$  a.u.

#### A. Energy-momentum map

The classical equilibrium solutions,  $r_e$ , of the effective potential (2) are given by the roots of the equation

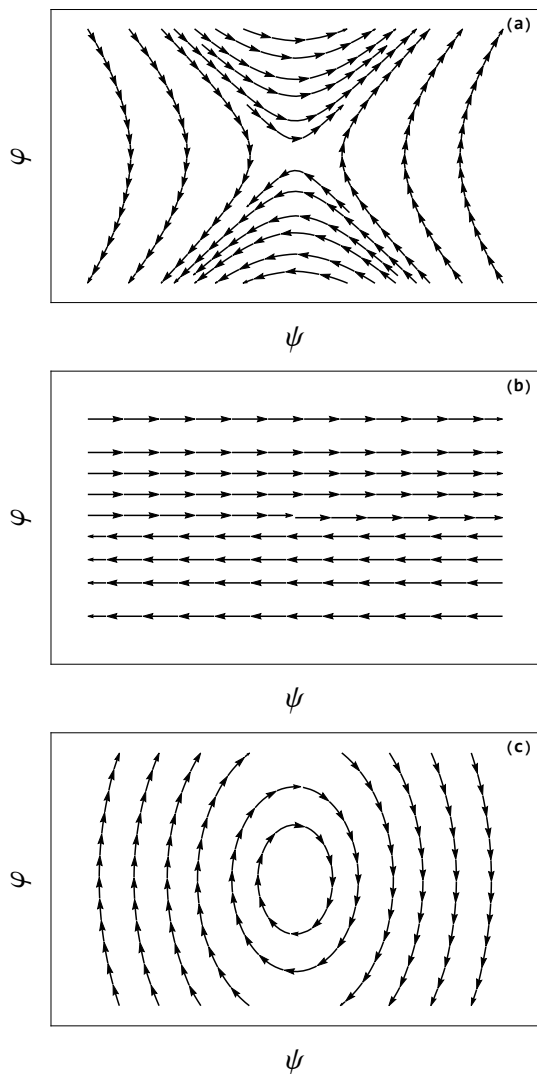


FIG. 2. Stream plots for trajectories in the vector field  $\dot{\Phi}$ . (a) Hyperbolic behavior in classically forbidden regions. (b) Behavior at classical turning points. (c) Elliptic behavior in classically accessible regions.

$dV_l(r)/dr = 0$  for  $l \geq 0$ . These roots can be seen as the zero contours of  $C(l, r) = dV_l(r)/dr$  in the  $l - r$  plane.

There are 2 types of equilibrium solutions for  $V_{l \neq 0}$ : stable equilibrium at the bottom of the potential well, and unstable equilibrium at the top of the centrifugal barrier. In the dissociative limit there is also a stable equilibrium for  $V_{l=0}$  and  $V_{l \neq 0}$ . The effective potential  $V_{l=0}$  does not have a centrifugal term and only the stable and the asymptotically stable equilibria are possible.

The zero contours,  $C(l, r) = 0$ , give the set equilibrium solutions as functions of the angular momentum  $r_e(l) = \{r_s(l), r_u(l)\}$ . The effective potential can be evaluated along  $r_s(l)$  and  $r_u(l)$  producing the curves

$$V_{s,u}(l) = V_l(r_{s,u}(l)), \quad (9)$$

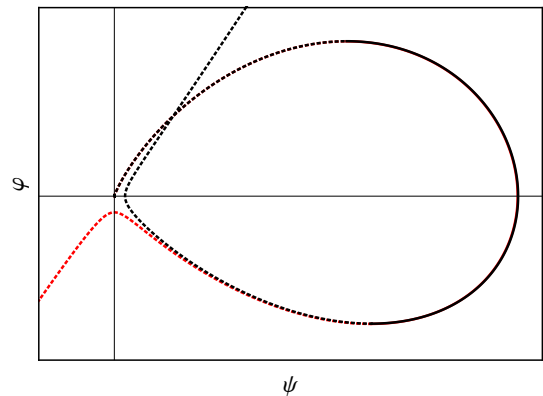


FIG. 3. Phase space trajectories for energies around the ground state,  $\mathcal{E}_0 \mp \Delta\mathcal{E}$  with  $l = 23$ . The black trajectory ( $\mathcal{E}_0 - \Delta\mathcal{E}$ ) diverges upwards meanwhile the red trajectory ( $\mathcal{E}_0 + \Delta\mathcal{E}$ ) diverges downwards.

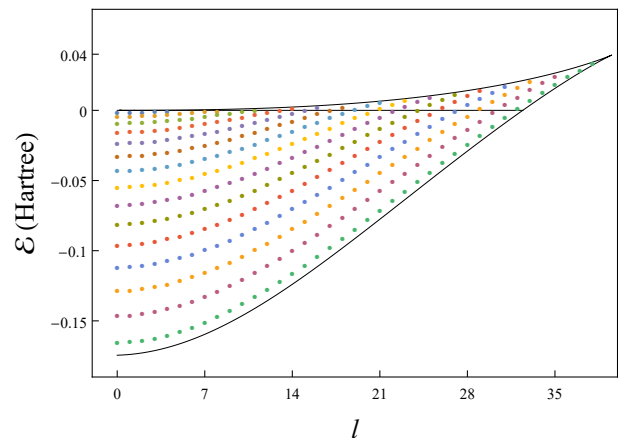


FIG. 4. Energy momentum diagram ( $\mathcal{E} - l$ ) for  $H_2$  molecule with angular momentum  $l$ . The classical equilibrium curves  $V_s(l)$  and  $V_u(l)$  are displayed as solid curves. The asymptotic equilibrium,  $V_a$ , is shown as a straight line with  $\mathcal{E} = 0$ . The lattice of quantum states is displayed with colored points. The color of the quantum states indicates vibrational quantum number.

on the  $\mathcal{E} - l$  plane [34]. Figure 4 shows the classical energy momentum equilibria for the effective potential  $V_l(r)$ . In the figure there are two curves forming a smile pattern,[35] and a straight line in black color. The lowest energy curve is clearly the stable equilibrium,  $V_s(l)$ , meanwhile the highest energy curve is the unstable equilibrium,  $V_u(l)$ . Between the stable and unstable equilibria there is a straight line with  $\mathcal{E} = 0$  representing the asymptotic stable equilibrium,  $V_a(l)$ . As the angular momentum increases the curves  $V_s(l)$  and  $V_u(l)$  approach each other until they finally join forming the right upper vertex observed in figure 4. This vertex indicates the highest possible value of  $l$  that can hold a potential energy well.

The curves for classical stable and unstable equilibria enclose an area that contains bound and resonance quan-

tum states. The line  $V_a(l)$  divides this area in two: the region for bound states with negative energy, and the region for resonance states with positive energy. These regions can be seen in figure 4, the points inside the regions are bound and resonance states, points with the same color have the same vibrational quantum number. The lattice of quantum states of figure 4 does not show quantum monodromy [35], at least for bound and resonance states.

### B. Arc length and winding number for finding bound and resonance states

It is convenient to use a polar representation of the trajectories:  $\rho = |\Phi|$ , and  $\theta = \arctan(\varphi/\psi)$ . The arc length  $\ell(\mathcal{E}) = \ell[\Phi(\mathcal{E})]$ , and the winding number  $w(\mathcal{E}) = w[\Phi(\mathcal{E})]$ , can be defined in terms of the one-parameter family of trajectories  $\Phi(\mathcal{E})$ :

$$\ell(\mathcal{E}) = \int_{r_i}^{r_f} |\dot{\Phi}(\mathcal{E})| dr, \quad (10a)$$

$$w(\mathcal{E}) = \frac{1}{2\pi} \int_{r_i}^{r_f} \dot{\theta} dr. \quad (10b)$$

Bound and resonance states are phase-space trajectories that minimize the arc length and the derivative of the winding number. The use of equations (3) in the integrand of  $\ell(\mathcal{E})$  gives

$$\ell(\mathcal{E}) = \int_{r_i}^{r_f} \sqrt{\varphi^2 + k_l^4 \psi^2} dr. \quad (11)$$

The winding number can be expressed in terms of  $\psi$  and  $\varphi$ ,

$$w(\mathcal{E}) = -\frac{1}{\pi\mu} \int_{r_i}^{r_f} \frac{h(\psi, \varphi, r)}{\rho^2} dr, \quad (12)$$

with  $h = h(\psi, \varphi, r)$  as the energy density

$$h(\psi, \varphi, r) = \frac{1}{2} (\mu\varphi^2 + \mu k_l^2 \psi^2). \quad (13)$$

The upper limit of the integrals (11) and (12),  $r_f$ , must be taken large enough to guarantee that trajectories reach the free region of the effective potential, for resonances. For the case of  $l = 23$ , figure 5 shows the derivative of the winding number  $w'(\mathcal{E})$  for negative and positive energies. There are 6 peaks for bound states with negative energy, and 2 peaks for resonance states with positive energy. The width of each resonance peak gives the lifetime of the resonance [36], for the  $l = 23$  case, lifetimes of  $1.23 \times 10^{-12}$  s and  $4.29 \times 10^{-13}$  s were obtained. The peak for the lowest energy resonance is very narrow with a long lifetime, meanwhile the peak for the higher energy resonance is broader with shorter lifetime. The background shown for positive energies in figure 5 depends on the upper limit of the propagation,  $r_f$  of equations (10). Although this background seems

to have a periodic structure, this feature depends mainly on computational aspects, as  $r_f$  takes higher values in the free region the intensity of the background increases and becomes noisier. Additional calculations were carried out for energies above the centrifugal energy barrier, there were not found resonances in the continuum.

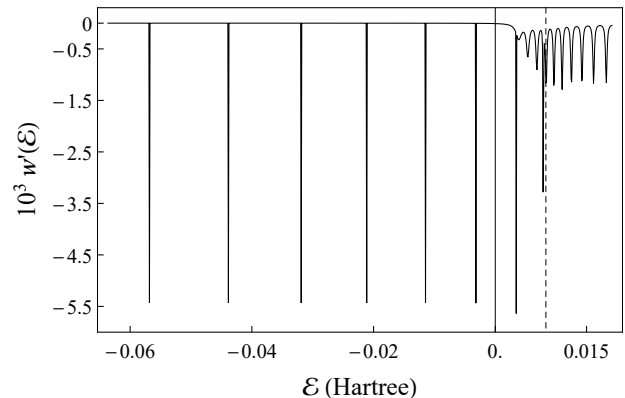


FIG. 5. Derivative of the winding number for  $l = 23$ . There are 6 bound states with negative energy and 2 resonances with positive energy. The energy for the top of the centrifugal barrier is displayed as a dashed vertical line.

Figure 6 displays the arc length (11) as a function of the energy for the Hydrogen molecule with  $l = 23$ . Bound states are shown as downwards peaks at negative energies. Resonance states are also shown as downwards peaks at positive energies. The inset of figure 6 shows that the peak of the first resonance is sharp and deep, as the peaks of bound states, while the peak of the second resonance is shallow. Figure 6 shows that for energy above the centrifugal barrier the arc length is a constant function of the energy.

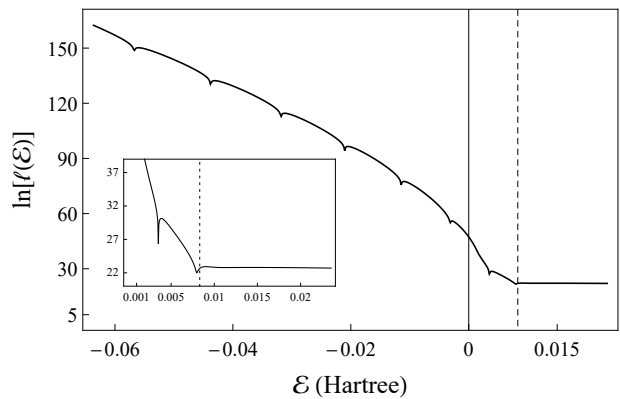


FIG. 6. Arc length as a function of the energy. The energy for the top of the centrifugal barrier is displayed as a dashed vertical line. The inset shows the resonances with more detailed. Logarithmic scale has been used for the ordinate.

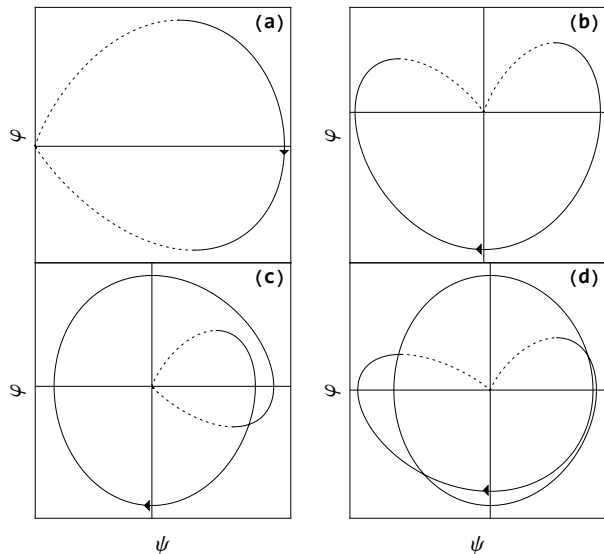


FIG. 7. Phase space trajectories of  $\text{H}_2$  with  $l = 23$  for vibrational eigenstates with (a)  $v = 0$ , (b)  $v = 1$ , (c)  $v = 2$ , and (d)  $v = 3$ . Solid (Dashed) line represent the part of the trajectory propagated on a classically allowed (forbidden) region.

### C. Phase-space representation of wave functions

The phase-space trajectories,  $\Phi_v = \Phi(\mathcal{E}_v)$ , for the lowest 4 bound states of Hydrogen molecule at  $l = 23$  are shown in figure 7. The trajectories  $\Phi_v$  are produced by the numerical propagation of equations (3) starting and ending closely near the fixed point,  $\Phi_v(r_i) \approx \Phi^*$ , and  $\Phi_v(r_f) \approx \Phi^*$ . These trajectories are not closed curves since the fixed point  $\Phi^*$  can not be used as initial condition and is never reached by the propagation regardless the value of  $r_f$ . The initial part of the propagation takes place in the classically forbidden region and follows the flow lines of the unstable manifold of figure 2(a), i.e., the initial direction of the trajectory follows the line extended along the unstable eigenvector  $\mathbf{e}_1 = \{\lambda_1^{-1}, 1\} = \{i/k_l, 1\}$ , with  $k_l = \sqrt{2\mu(\mathcal{E} - V_l(r_i))}$ , and  $l = 23$ . Since the initial value of  $r$ ,  $r_i$ , is classically inaccessible, the unstable eigenvector takes the value  $\mathbf{e}_1 = \{1/\sqrt{2\mu|\mathcal{E} - V_l(r_i)|}, 1\} \approx \{0^+, 1\}$ . The trajectories in the panels of figure 7 show this initial part of the propagation as the dashed curve that connects the origin with a point to the right in the upper half of the plane. The propagation continues in the classically accessible region producing the solid curves of figure 7, these curves circulate in clockwise direction. Finally there is a transition to the external (right) classical forbidden region, which is represented by the dashed curve approaching to the fixed point  $\Phi^*$  from the left along the stable manifold, i.e., along the line generated by the stable eigenvector  $\mathbf{e}_2 = \{-1/\sqrt{2\mu|\mathcal{E} - V_l(r_f)|}, 1\}$ , with  $l = 23$ .

The phase space trajectories,  $\Phi_6$  and  $\Phi_7$ , for the 2 resonance states of Hydrogen with  $l = 23$  are shown in figure

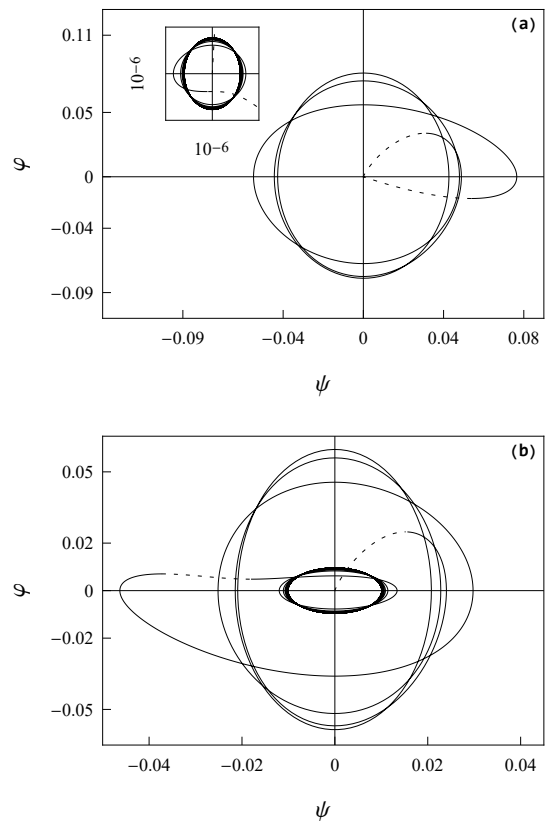


FIG. 8. Phase space trajectories for the resonance states of  $\text{H}_2$  with  $l = 23$ . (a)  $v = 6$ , (b)  $v = 7$ . The inset of panel (a) shows the oscillatory behavior for large values of  $r$ .

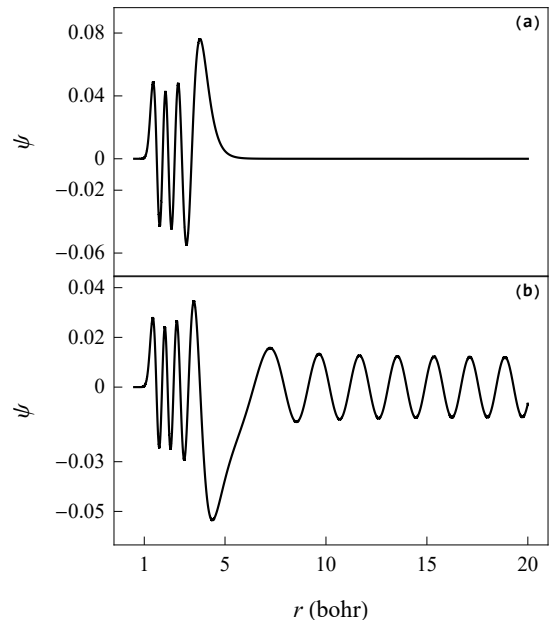


FIG. 9. Radial wave functions for the (a)  $l = 23$ ,  $v = 6$  and (b)  $l = 23$ ,  $v = 7$  resonances.

8. The trajectories for resonance states circulate in clockwise direction, as bound states. Figure 8(a) displays the phase space trajectory for the lower energy resonance,  $\Phi_6$ . The first resonance displays a strong character of bound state, starting and ending very close to the fixed point  $\Phi^*$ ; however, as it is shown in the inset of the figure, the trajectory does not approach  $\Phi^*$  but falls in cycle with small amplitude. The trajectory for the second resonance is shown in figure 8(b). The second resonance start near  $\Phi^*$  and behaves in oscillatory fashion as a bound state, the trajectory then crosses the centrifugal barrier in an almost vertical line and finally falls in a cycle with considerable amplitude. The second resonance displays a mixed character of bound state and plane wave. The wave functions  $\psi_v(r)$  for the resonances are shown in figure 9, for the sake of comparison. Panel 9(a) shows the low energy resonance, it is clear from the figure that this resonance resembles a bound state with almost imperceptible oscillations for large values of  $r$ . The higher energy resonance is shown in figure 9(b) where again is evident its mixed character between a bound state and a plane wave.

#### IV. CONCLUDING REMARKS

This phase-space propagation scheme displays advantages over spectral and pseudospectral methods, like

DVR or FGH, for calculating bound and resonance states. Since phase-space propagation is an initial value method, there is not imposition of artificial boundary conditions or adjustable absorbing potentials. The energy momentum map allows to have a global view of the quantum states and its relationship with the classical equilibria. The stability analysis of the phase-space structure allows to get important information that can be related with the features of the wave function in classically allowed or forbidden regions. Bound states behave as classical unstable periodic orbits meanwhile resonance states behave as stable cycles. The use of the arc length and the winding number as functions of the energy, for the same initial condition, produces spectra with peaks centered at the exact energies of bound and resonance states. The width of the resonance peaks allows to estimate the lifetime of the resonances and it is related to the bound/continuum character of the resonance. Broad peaks are related to resonances with strong bound state character meanwhile narrow peaks are related to resonances with stronger character of continuum states.

#### V. ACKNOWLEDGMENTS

This project has been fully financed by the internal research grants of Universidad Icesi.

- 
- [1] E. Schrödinger, Phys. Rev. **28**, 1049 (1926).
  - [2] W. Derrick and S. I. Grossman, *Elementary Differential Equations*, 4th ed. (Pearson, 1997).
  - [3] P. Atkins and R. S. Friedman, *Molecular Quantum Mechanics*, 5th ed. (Oxford, New York, NY, USA, 2011).
  - [4] R. J. LeVeque, *Finite difference methods for ordinary and partial differential equations: steady state and time dependent problems*, 1st ed. (SIAM, Philadelphia, PA, USA, 2007).
  - [5] H. E., S. P. Nørset, and G. Wanner, *Solving Ordinary Differential Equations I: Nonstiff Problems*, 2nd ed. (Springer-Verlag, Berlin, 2009).
  - [6] H. E. and G. Wanner, *Solving Ordinary Differential Equations II: Stiff and Differential-Algebraic Problems*, 2nd ed. (Springer-Verlag, Berlin, 1996).
  - [7] D. J. Tannor, *Introduction to Quantum Mechanics: a time dependent perspective*, 5th ed. (University Science Books, Sausalito, CA, USA, 2007).
  - [8] J. C. Light, I. P. Hamilton, and J. V. Lill, J. Chem. Phys. **82**, 1400 (1985).
  - [9] D. T. Colbert and W. H. Miller, J. Chem. Phys. **96**, 1982 (1992).
  - [10] J. S. Molano, K. D. Pérez, J. C. Arce, J. G. López, and M. L. Zambrano, Phys. Rev. A **100**, 063407 (2019).
  - [11] C. C. Marston and G. G. BalintKurti, J. Chem. Phys. **91**, 3571 (1989).
  - [12] S.-I. Chu, Chem. Phys. Lett. **167**, 155 (1990).
  - [13] Y. G. and C. S.-I, Chem. Phys. Lett. **204**, 381 (1993).
  - [14] J. N. Bardsley, Int. J. Quantum Chem. **14**, 343 (1978).
  - [15] N. Moiseyev and C. Corcoran, Phys. Rev. A **20**, 814 (1979).
  - [16] J. Muga, J. Palao, B. Navarro, and I. Egusquiza, Phys. Rep. **395**, 357 (2004).
  - [17] A. Landau, I. Haritan, P. R. Kaprlov-nsk, and N. Moiseyev, Mol. Phys. **113**, 3141 (2015).
  - [18] J. P. Boyd, Comput. Phys. **4**, 83 (1990).
  - [19] J. P. Boyd, *Chebyshev and Fourier Spectral Methods*, 2nd ed. (Dover publications, Mineola, NY, USA, 2000).
  - [20] H. Alici and H. Taşeli, Appl Numer Math **87**, 87 (2015).
  - [21] H. Alici, Hacet. J. Math. Stat. **49**, 539 (2020).
  - [22] V. Arnol'd, *Ordinary Differential Equations* (Springer-Verlag, Heidelberg, Germany, 1992).
  - [23] B. Numerov, Astron. Nachr. **230**, 359 (1927).
  - [24] H. Kobeissi and M. Kobeissi, J. Comput. Phys. **77**, 501 (1988).
  - [25] T. E. Simos, Int. J. Quantum Chem. **62**, 467 (1997).
  - [26] V. Tselyaev, J. Comput. Appl. Math. **170**, 103 (2004).
  - [27] J. Vigo-Aguiar and H. Ramos, J. Math. Chem. **37**, 255 (2005).
  - [28] M. Pillai, J. Goglio, and T. G. Walker, Am. J. Phys. **80**, 1017 (2012).
  - [29] K. Kodaira, Am. J. Math. **71**, 921 (1949).
  - [30] S. Strogatz, *Nonlinear Dynamics and Chaos* (Addison-Wesley, Reading, MA, 1994).
  - [31] J. S. Sims and S. A. Hagstrom, J. Chem. Phys. **124**, 094101 (2006).
  - [32] L. Wolniewicz, J. Chem. Phys. **99**, 1851 (1993).

- [33] L. Wolniewicz, I. Simbotin, and A. Dalgarno, *Astrophys. J. Suppl. S.* **115**, 293 (1998).
- [34] C. A. Arango, *Classical and Semiclassical Mechanics of Molecular Rotors in Tilted Fields*, Ph.D. thesis, Cornell University (2005).
- [35] C. A. Arango, W. W. Kennerly, and G. S. Ezra, *Chem. Phys. Lett.* **392**, 486 (2004).
- [36] K. D. Pérez, J. C. Arce, and J. G. López, *Astrophys. J. Suppl. S.* **243**, 1 (2019).